PROCEEDINGS OF SPIE

2D materials integrated in Si₃N₄ photonics platform

Joaquin Faneca, Benjamin T. Hogan, E. Torres Alonso, Monica Craciun, Anna Baldycheva

Event: SPIE OPTO, 2018, San Francisco, California, United States

SPIE.

2D materials integrated in Si_3N_4 photonics platform

Joaquin Faneca[1, 2], Benjamin T. Hogan[1, 2], E. Torres Alonso[1], Monica Craciun[1] and Anna Baldycheva[1]

[1]University of Exeter, College of Engineering Mathematics and Physical Sciences, Exeter, EX4 4QF, UK
[2]EPSRC Centre for Doctoral Training in Electromagnetic Metamaterials University of Exeter, EX4 4QL, UK

ABSTRACT

In this paper, we discuss a back-end CMOS fabrication process for the large-scale integration of 2D materials on SOI (silicon-on-insulator) platform and present a complete theoretical study of the change in the effective refractive index of 2D materials-enabled silicon nitride waveguide structures. The chemical vapour deposition (CVD) and liquid exfoliation fabrication methods are described for the fabrication of graphene, WS_2 and MoS_2 thin films. Finite-difference frequency-domain (FDFD) approach and the Transfer Matrix Method were used in order to mathematically describe these structures. The introduction of thin films of 2D material onto Si_3N_4 waveguide structures allows manipulation of the optical characteristics to a high degree of precision by varying the Fermi-level through the engineering of the number of atomically thin layers or by electrical tuning, for example. Based on the proposed tuning approach, designs of graphene, WS_2 and MoS_2 enabled Si_3N_4 micro-ring structures are presented for the visible and NIR range, which demonstrate versatility and desirable properties for a wide range of applications, such as bio-chemical sensing and optical communications.

1. INTRODUCTION

Integrated silicon nitride (Si_3N_4) structures are a very promising platform for the development of waveguides and micro-rings due to their low nonlinearity[1] and the transparency that they possess in the infrared and visible ranges[2,3]. Si_3N_4 waveguides have been widely employed for light propagation in the near infrared and visible ranges of the electromagnetic spectrum. Si waveguides provide more confined modes than the Si_3N_4, possibly leading to more compact devices. However, Si_3N_4, as a deposited material is more cost effective and provides more freedom in the positioning of the 2D material sheets [4].

Light modulation is crucial in optical communications interconnects and WDM (wavelength division multiplexers). High performance light modulation solutions are becoming technologically indispensable. The emergence of 2D materials' technology to achieve ultrafast, low-loss, and broadband optical signal processing in simple configurations looks set to greatly enhance light modulation devices. In this paper we discuss large-scale integration of 2D materials as graphene or transition metal dichalcogenides (TMDs) such as MoS_2 and WS_2 on a 4-inch wafer Si photonics platform.

In this work we discuss the different methods for the large-scale integration of 2D materials, while the individual thickness control of each flake can be performed using the back-end laser thinning fabrication approach reported recently[5,6]. The obtained results demonstrate potential for realisation of truly reconfigurable electronic-photonic devices with a wide range of applications such as biosensors, neuroscience, wavelength division multiplexing and modulators for optical communication interconnects[7].

2. INTEGRATION OF 2D MATERIALS ON Si_3N_4 PHOTONICS PLATFORM

Several methods have been developed by which 2D materials can be exfoliated, each with their own advantages and disadvantages. Firstly, a mechanical cleavage method can be used (the so-called 'sticky-tape' method) where layers are separated by coupling one layer to a sticky surface and mechanically peeling it away from the bulk[8]. This method produces

very pure materials with few defects induced and can also give relatively large areas of material coverage. However, this method has poor scalability and production of large quantities of 2D material is extremely time intensive. Alternatively, a vapour deposition method can be used where a 2D material is grown directly on a substrate from vaporized precursor molecules at very high temperatures[9–12]. This method can produce large areas of 2D material and can be scaled to produce large quantities. However, there are numerous sources for the introduction of defects in the material including substrate induced defects and impurities in the vapours used amongst others, the material must be transferred from the substrate after deposition which can be problematic, and the production cost and time are prohibitive to adoption at larger scales. Adoption of 2D materials in novel device applications, is often limited by challenges surrounding the scalability, cost of production processes or limited quality of materials produced. In this work, two different deposition methods have been explored:

2.1 Liquid Exfoliation deposition: In liquid phase exfoliation, a bulk material is dispersed in a solvent and then the individual constituent layers are broken apart[14–18]. In the standard liquid phase exfoliation processes, which is demonstrated in Figure 1, the bulk material layers are broken apart using ultrasonication [Fig. 1(c)], where high frequency sound waves are transmitted through the solution[14–17,19–22]. The sound waves induce the formation of bubbles and cavities between layers which break the layers apart as they expand. However, they also cause additional intralayer strains in the material which cause cleavage of the particles, reducing the size of the particles obtained after exfoliation. The use of intercalating surfactants to weaken the interlayer forces before exfoliation can greatly increase the yield of the exfoliation[14,16], but the subsequent removal of the surfactant is liable to damage the quality of the exfoliated product. Other than ultrasonication, other methods have been developed for liquid phase exfoliation, including strong acid induced oxidation reactions causing cleavage[23] and freezing of water intercalated layered structures where expansion of water as it freezes causes interlayer cleavage[24]. Following on from the exfoliation, particles of specific sizes can be isolated through high speed centrifugation of the dispersion[25,26] [Fig. 1(d)], solvent induced selective sedimentation[27] or by pH-assisted selective sedimentation[28] amongst others. Fractionation [Fig. 1(e)] then allows selection of a suitable range of particle sizes depending on the application, with homogeneous distributions of particle sizes obtainable [Fig. 1(f)]. A significant advantage of using liquid phase exfoliation is the possibility of obtaining liquid crystal phase dispersions through the careful selection of size and concentration of the dispersed particles[29]. Liquid crystal phase dispersions facilitate the deposition of films with greater uniformity[29]. In this work, graphene was produced from graphite by exfoliation in water, using sodium cholate as a surfactant. Dispersions were ultrasonicated for around 5 hours, and centrifuged for 5 mins at 2000 rpm to separate out any unexfoliated particles from the solution. An aliquot containing all the non-sedimented particles was then transferred and used for further processes. A similar process was used for the exfoliation of transition metal dichalcogenides. In these cases, isopropanol was used as the solvent and no surfactant was required. Ultrasonication processes and ultracentrifugation where carried out for the same times and speeds. The resultant dispersions of exfoliated 2D materials were then filtered through polytetrafluoroethylene (PTFE) membranes to produce thin films on the membrane. These films can then be readily transferred to other substrates as requirement.

(a)　(b)　(c)　(d)　(e)　(f)

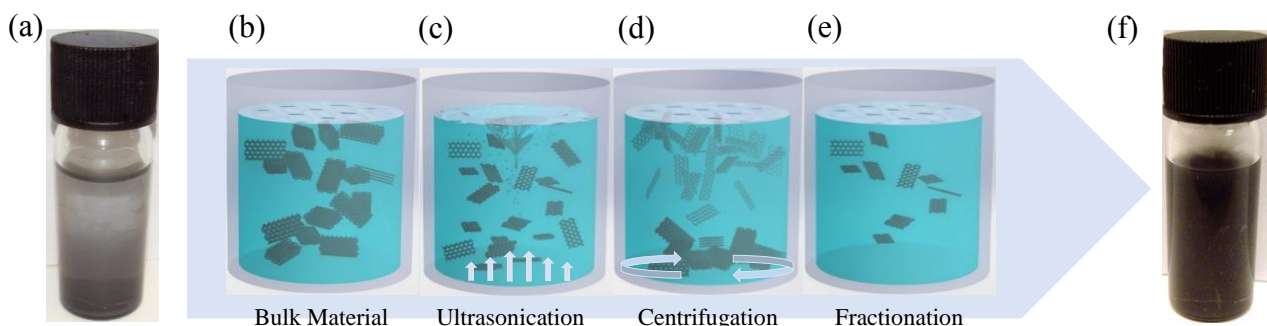Bulk Material　　Ultrasonication　　Centrifugation　　Fractionation

Figure 1: a) A dispersion of bulk material. b) Schematic of the liquid phase exfoliation of bulk layered materials to low- or two-dimensional particles. (bulk material) c) ultrasonication is used to exfoliate down to smaller flake sizes. d) Centrifugation then aggregates the largest particles, with the smallest remaining suspended in the solution. e) Fractionation then allows the selection of aliquots containing f) the resultant homogeneous distributions of similarly sized particles.

2.2 CVD (Chemical vapour deposition) technique graphene deposition. The CVD technique is based on diffusing gaseous carbon into the nickel substrate, and then forcing it to precipitate out by cooling the nickel. The thickness and crystalline ordering of the precipitated carbon is controlled by the cooling rate and by the concentration of carbon dissolved in the nickel. This concentration is in turn controlled by the type and concentration of the carbonaceous gas, and the thickness of the nickel layer. After chemically etching the nickel, the graphene membrane detaches and can be transferred to another substrate. This direct CVD synthesis provides high quality layers of graphene without intensive mechanical or chemical treatments. [13]

2.3 Back-end CMOS fabrication process for the large-scale integration of 2D materials on SOI (Silicon-on-insulator) platform. In this paper, the fabrication methods discussed above were used to integrate 2D material thin films on Si_3N_4 photonic wafers. In the first step, e-beam lithography followed by inductively coupled plasma reactive ion etching (JLS RIE) was used to fabricate waveguide and micro-ring devices from a 150nm-thick Si_3N_4 layer, supported on a SiO_2 bottom cladding layer of 2 µm (Figure 2 (a)). We used a TI PRIME adhesion promoter and MaN 2403 e-beam resist to allow patterns to be designed using a NBL e-beam system, followed by post exposure bake for 90 seconds at 90°C to reflow the resist surface and reduce sidewall roughness. The etching was performed with a CHF_3/O_2 reactive gas mixture. 2D materials thin films were deposited using back-end processes. Above the Si_3N_4 photonic layer, a 1µm thick photoresist was produced via spin-coating. This was followed by pattering using a laser writing method with a precision of 0.6µm and wet etching of defined structures and trenches within the photoresist layer, down to the photonic layer [Fig. 2(b-c)]. With the photoresist removed from the required areas, CVD or liquid exfoliated 2D materials were transferred onto the top of the wafer [Fig 2(d)]. After removal of the photoresist mask, final individual devices with specific, micron-size structures of 2D materials- as desired and designed- were achieved [Fig. 2(e-f)].
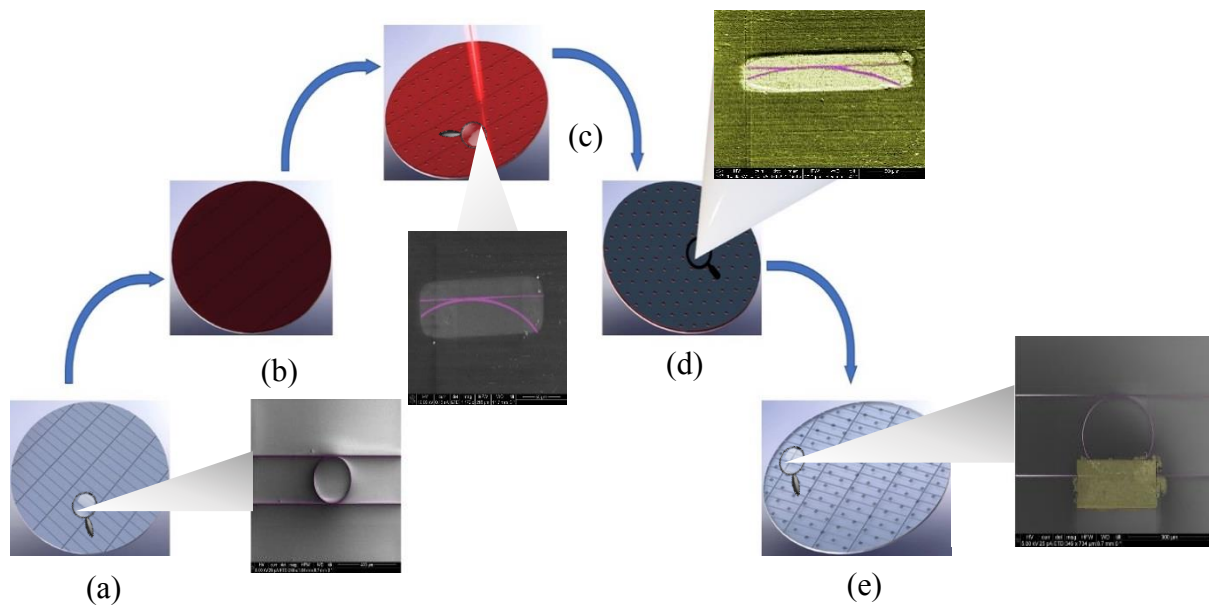

Fig 2. **Back-end CMOS fabrication process flow.** (a) SOI wafer with photonic microchips. (b) Photoresist deposition on the photonics wafer. (c) Development of micro-trenches and other structures within the photoresist layer, down to the photonic waveguide layer. (d) Wafer scale transfer of 2D material thin film. (e) SOI photonic wafer with integrated 2D materials into the photonic circuits after photoresist removal.

3   2D MATERIALS ENABLED PASSIVE PHOTONIC STRUCTURES IN THE VISIBLE RANGE

The thickness of the different 2D materials deposited on top of the different Si_3N_4 structures can be controlled. A complete study of how the width and the thickness of the different 2D materials can affect the TE mode which propagates along a standard silicon nitride waveguide with the dimensions of width W_{wg} =1.2 μm and thickness h_{wg} = 0.3 μm is discussed [Fig.3] giving rise to the possibilities for different 2D materials modulators and filters.
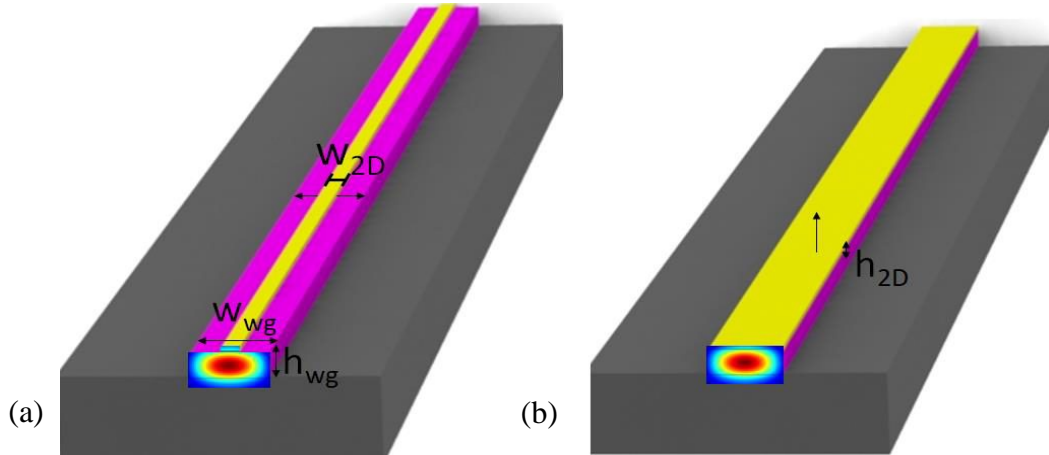

Fig 3. Schematic of different 2D materials flakes dimensions, using different 2D materials width (a) and thickness (b) on the top of a standard Si_3N_4 waveguide of W_{wg} =1.2 μm width and h_{wg} =0.3 μm thick.

3.1 Graphene

Graphene, a single layer of graphite, was the first experimentally demonstrated two-dimensional material. Graphene has been extensively studied due to its unique mechanical, thermal, electronic and optical properties. The linear structure of the dispersion leads to the universal optical conductance of the interband transition[30], which has been experimentally confirmed[31]. Single-layer graphene absorbs 2.3% of perpendicularly incident light within the infrared-to-visible spectral range. The absorption coefficient is precisely defined by $e^2/\hbar c$, the fine-structure constant.

The special behaviour of graphene is due to its 2D structure that confines electrons in one atomic layer, and also due to the low density of states (DOS) near the Dirac points, which causes the Fermi energy to shift significantly with variation of the carrier density[32]. For example, a Fermi level up to 0.9 eV has been experimentally demonstrated using the electrostatic field gating technique[33]. The tuneable bandgap of graphene offers great opportunities and flexibility for infrared and visible light manipulation.

A parametric sweep in thickness and width has been studied. By changing the dimensions of the flakes deposited on top of the waveguides, a change in the effective refractive index is observed, and consequently a modulation of the signal. In [Fig. 4(a-b)] the alteration of the effective refractive index in the visible range is plotted. As can be seen, graphene shows a continuous change in the effective refractive index as a function of both parameters. The absorption coefficient in the graphene goes from being a transparent material with no absorption up to 0.016 and the real part of the refractive index changes $4 \cdot 10^{-3}$. The proposed designs are based on coupled micro-resonator structures, using the Transfer Matrix Method developed by Yariv [34] we calculated the drop-port transmission spectra of a micro-ring-resonator-based add–drop filter. For a radius R = 6 μm, α = 2 cm^{-1}, and coupling coefficient κ = 0.4, when the thickness of the graphene is equal to 1 nm and the width to 50 nm, the effective refractive index is $n_{eff} = 1.856 + 1.2 \cdot 10^{-4}i$ corresponding to a resonant wavelength of 0.7 μm. Increasing the thickness up to 8nm and the width up to 1.2μm of the graphene flake, an effective refractive index of 1.86+0.016i is given and a resonant wavelength of 0.716 μm is found [Fig. 4(c)]. Hence, modifying the thickness and width

of the graphene flakes deposited on the top of waveguides, a 0.23% shift in the resonance of the micro-ring resonator structure [Fig. 4(d)] is achieved.
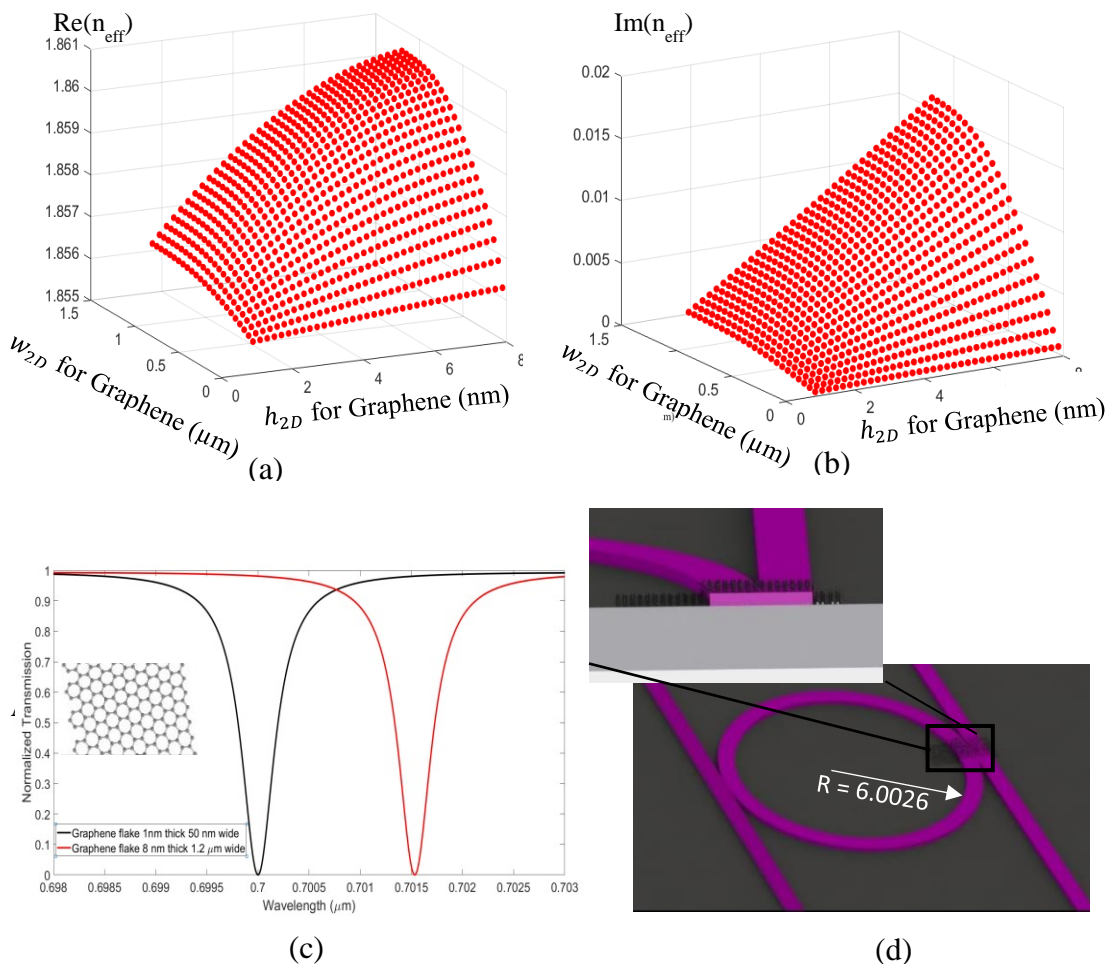

(a)

(b)

(c)

(d)

Fig. 4 (a) Real part of the effective refractive index for different widths and thicknesses of graphene. (b) Imaginary part of the effective refractive index for different width and thicknesses of graphene. (c) drop-port transmission spectra of a micro-ring-resonator-based add–drop filter with a radius R = 6.0026 μm, $\alpha = 2$ cm−1, and coupling coefficients $\kappa = 0.4$ for a graphene flake of 1 nm thick and 50 nm wide (black line) and for a graphene flake of 1.2 um wide (covering all the waveguide) and 8 nm thick (red line). (d) Add-drop filter schematic for graphene flakes.

3.2 Transition Metal Dichalcogenides (TMDs)

2D TMDs are atomically thin semiconductors of the type MX_2, where M is a transition metal atom and X is a chalcogen (group 16) atom. Typically, TMDs have bandgaps ranging from 1 to 2.5 eV, corresponding to near-infrared or visible frequencies. One of the most important properties of these materials is the transition from an indirect to a direct bandgap that occurs when the material thickness decreases from multilayer to monolayer. This evolution of the band structure results from changed confinement effects and the negation of the interaction with neighbouring layers. Unlike the universal optical

conductance in graphene, the semiconducting TMD may exhibit multiple absorption peaks from ultraviolet to near infrared frequencies due to excitonic and inter-band transitions.

3.2.1 WS₂

In the case of WS$_2$, the effective refractive index for a 1nm thick and 50 nm wide flake is $n_{eff} = 1.855 + 2.255 \cdot 10^{-5}i$ corresponding to a resonant wavelength of 0.7 μm . Increasing the thickness and the width of the flake up to 8nm and 1.2 μm respectively, the change in the real part of the effective refractive determined for the studied range is 0.023 [Fig. 5(a)]. The imaginary part increases to $3 \cdot 10^{-3}$ [Fig. 5(b)], a resonant wavelength of 0.698 μm is found corresponding to a 0.13% shift in the resonance of the add-drop filter. [Fig. 5(c)]. Using micro-ring resonators [Fig. 5(d)] with R=6μm, quality factors (Q) of the order of $10^2 - 10^3$ are achieved. Increasing the radius of the micro-ring a reduction in the scattering losses is obtained and an increase of at least two orders of magnitude in the quality factor, up to $10^5 - 10^6$ for radii on the order of 50 µm, can be obtained.
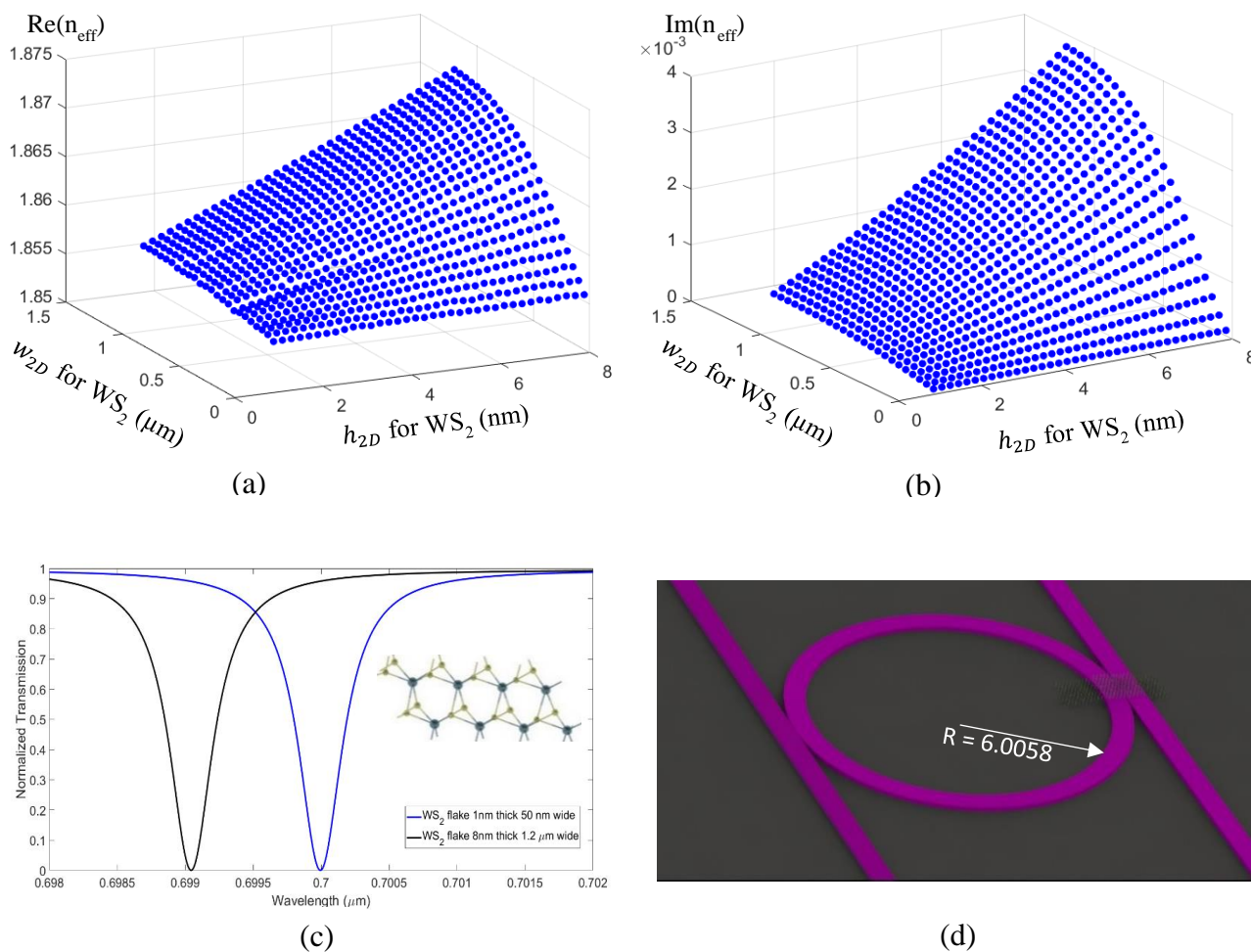

(a)

(b)

(c)

(d)

Fig. 5 (a) Real part of the effective refractive index for different WS₂ widths and thicknesses. (b) Imaginary part of the effective refractive index for different WS₂ widths and thicknesses. (c) drop-port transmission spectra of a micro-ring-resonator-based add–drop filter with a radius R = 6.0058 µm, α = 2 cm−1, and coupling coefficients $\kappa = 0.4$ for a WS₂ flake of 1 nm thick and 50 nm wide (black line) and for a graphene flake of 1.2 um wide (covering all the top waveguide) and 8 nm thick (blue line). (d) Add-drop filter schematic for WS₂ flakes.

3.2.2 MoS₂

In the case of using MoS₂, the effective refractive index for a 1nm thick and 50 nm wide flake is $n_{eff} = 1.851 + 5.4 \cdot 10^{-5}$ corresponding to a resonant wavelength of $0.7 \ \mu m$ for a $6.0188 \ \mu m$ radius. Increasing the thickness and the width of the flake up to 3.8 nm and $1.2 \ \mu m$ respectively, the change in the real part of the effective refractive for the studied range is 0.041 [Fig. 6(a)]. The imaginary part increases to $1 \cdot 10^{-2}$ [Fig 6(b)], a resonant wavelength at $0.7015 \ \mu m$ is found for this value, corresponding to a 0.21% shift in the resonance of the add-drop filter [Fig. 6(c-d)].
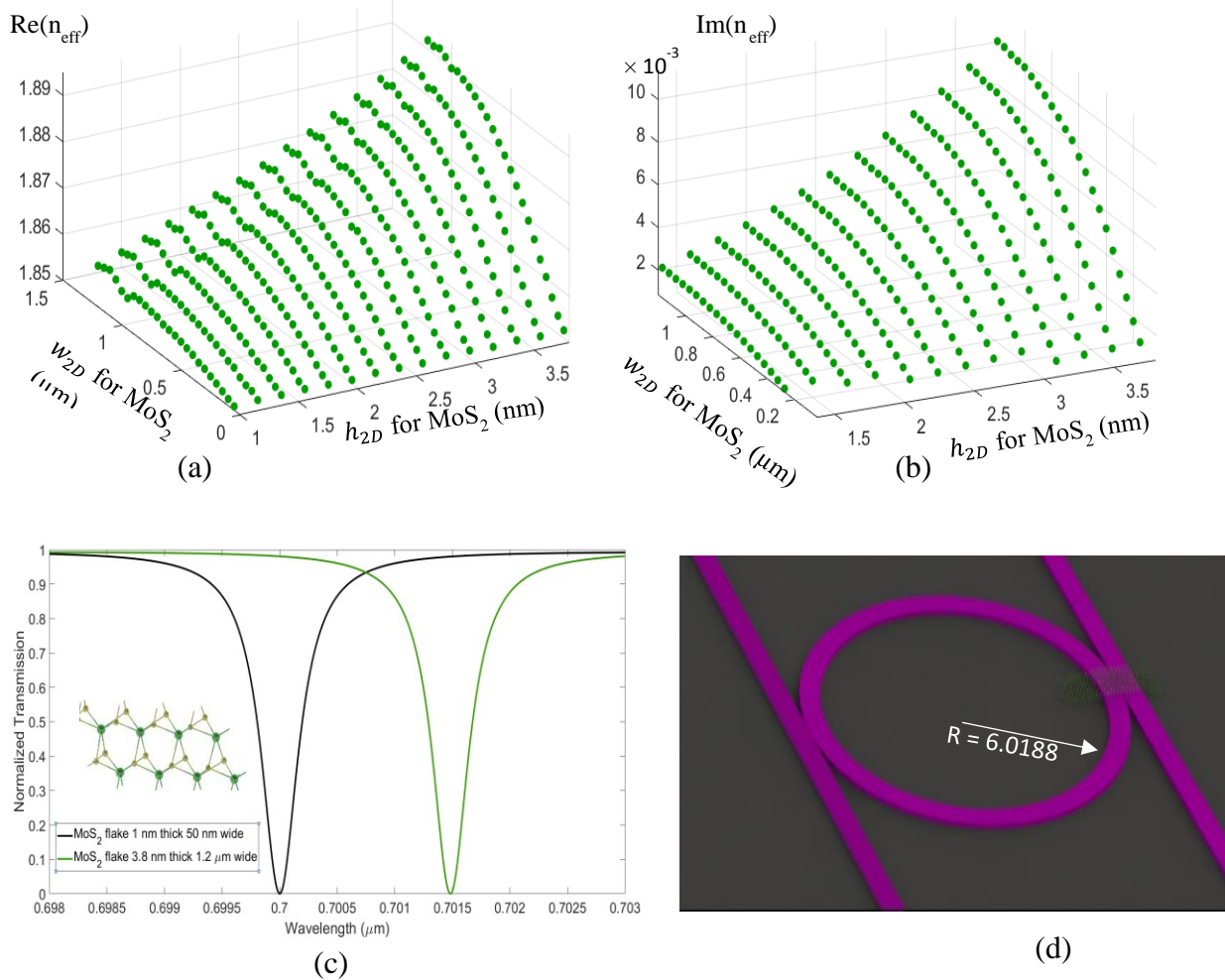

Fig. 6 (a) Real part of the effective refractive index for different MoS₂ widths and thicknesses. (b) Imaginary part of the effective refractive index for different MoS₂ widths and thicknesses. (c) Drop-port transmission spectrum of a micro-ring-resonator-based add–drop filter with a radius R = 6.0188 µm, α = 2 cm−1, and coupling coefficients κ = 0.4 for a MoS₂ flake of 1 nm thick and 50 nm wide (black line) and for a graphene flake of 1.2 um wide (covering all the top waveguide) and 3.8 nm thick (green line). (d) Add-drop filter schematic for MoS₂ flakes.

4 2D MATERIALS ENABLED TUNEABLE STRUCTURES FOR OPTICAL COMMUNICATION APPLICATIONS

For a complete study of tuneable devices at optical communications wavelengths, the optical properties of graphene should be defined. One of the most important properties of graphene is its gate-variable optical conductivity[35].

The graphene conductivity can be tuned by applying drive voltages which will change the carrier density of graphene and, consequently, the Fermi level. The dependence of graphene's optical conductivity on inter- and intra-band transitions has been analytically derived at 0K and at 300K [36]. The complex optical conductivity $\sigma(\omega, \mu, \Gamma, T)$ depends on the angular frequency ω, chemical potential μ, charge particle scattering rate being τ the relaxation time $\Gamma = \tau^{-1}$ and finally T is the temperature. [37] The dynamic optical conductance response of graphene can be derived from the Kubo formula:

$$\sigma_{total}(w, \mu, \Gamma, T) = \sigma_{intra} + \sigma'_{inter} + i\sigma''_{inter} \tag{1}$$

The intra-band conductivity σ_{intra} has the Drude form

$$\sigma_{intra} = \frac{\sigma_0 4\mu}{\pi} \cdot \frac{1}{\hbar\tau_1^{-1} - i\hbar\omega} \tag{2}$$

where $\sigma_0 = \frac{\pi e^2}{2h} = 60.8\ \mu s$ is the universal optical conductance and τ_1^{-1} is the relaxation rate associated with intra-band transitions. The inter-band contribution has the form:

$$\sigma'_{inter} = \sigma_0(1 + \frac{1}{\pi}\arctan\frac{\hbar w - 2\mu}{\hbar\tau_2^{-1}} - \frac{1}{\pi}\arctan\frac{\hbar w + 2\mu}{\hbar\tau_2^{-1}}) \tag{3}$$

and

$$\sigma''_{inter} = -\frac{\sigma_0}{2\pi}\ln\frac{(2\mu + \hbar\omega)^2 + \hbar^2\tau_2^{-2}}{(2\mu - \hbar\omega)^2 + \hbar^2\tau_2^{-2}} \tag{4}$$

where τ_2^{-1} is the relaxation rate associated with inter-band transitions. The complex dielectric function $\varepsilon(\mu)$ can be obtained from the complex optical conductivity of graphene described by

$$\varepsilon(\mu) = 1 + \frac{i\sigma(\mu)}{\omega\varepsilon_0\delta} \tag{5}$$

where $\delta = 0.7\ or\ 0.4\ nm$ is the graphene thickness layer and ε_0 is the permittivity of vacuum. For further calculations, $\lambda = 1550\ nm$, T=296K, $\tau_1 = 10\ fs$ and τ_2= 1.2 ps were chosen. In [Fig 7] The dielectric dependence with the change in the Fermi level has been plotted, a parametric sweep of the Fermi level from 0 eV up to 1eV has been studied for different graphene flake thicknesses.
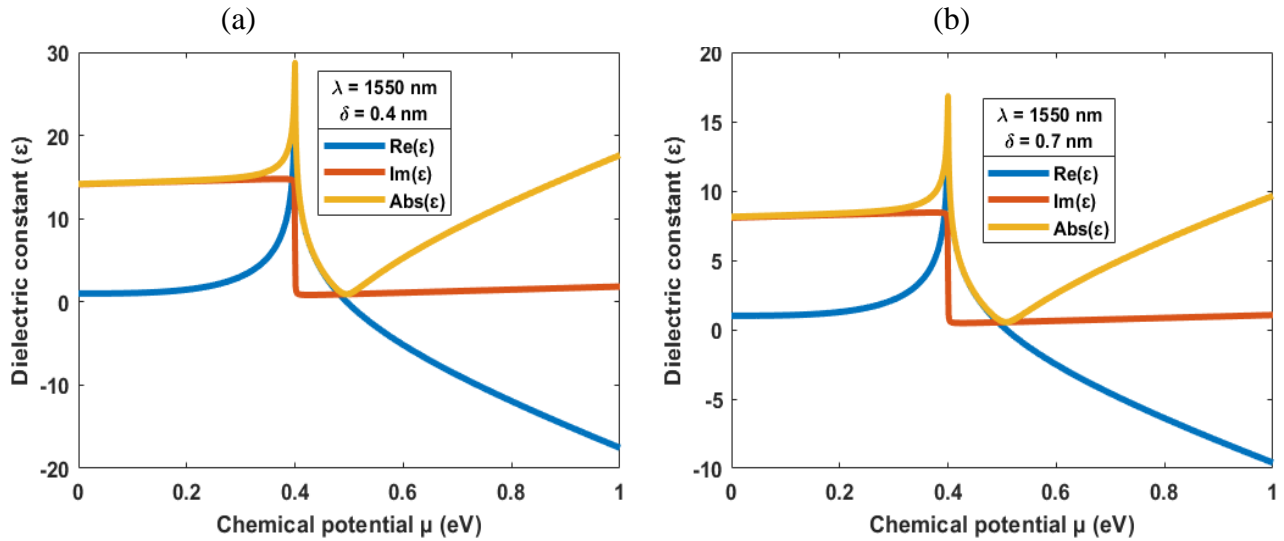
Fig. 7 (a) Calculated dielectric constant of graphene (real part, imaginary part and magnitude) as function of chemical potential μ of graphene for $\lambda = 1550\ nm$ for a 0.4 nm thick graphene flake. (b) Calculated dielectric constant of graphene (real part, imaginary part and magnitude) as function of chemical potential μ of graphene for $\lambda = 1550\ nm$ for a 0.7 nm thick graphene flake.

When the chemical potential varies from 0.4 eV to 0.6 eV, the dielectric constant shows a significant change. In the case of 0.4 nm thick graphene, a change from $\varepsilon(0.4eV) = 14.21 + 14.65i$ to $\varepsilon(0.6eV) = -5.168 + 1.111i$ is observed. Using Comsol Multiphysics, the effective refractive index associated to both Fermi level values $n_{eff}(0.4eV) = 1.5355 - 1.735\ 10^{-3}i$ and $n_{eff}(0.6eV) = 1.5332 - 1.\ 289 \cdot 10^{-4}i$ has been calculated . In the case of a 0.7 nm thick flake, the change in the dielectric constant goes from $\varepsilon(0.40eV) = 9.097 + 8.334i$ to $\varepsilon(0.60eV) = -2.492 + 0.6322i,$ and consequently the effective refractive index goes from $n_{eff}(0.4eV) = 1.5356 - 1.\ 7277 \cdot 10^{-3}i$ and $n_{eff}(0.6eV) = 1.5333 - 1.\ 2943 \cdot 10^{-4}i$. Using these values, a 0.148% shift in the resonance of the add-drop filter for a 0.4 nm graphene flake is achieved [Fig. 8(a)], and 0.148% in the case of a 0.7nm flake [Fig. 8(b)].
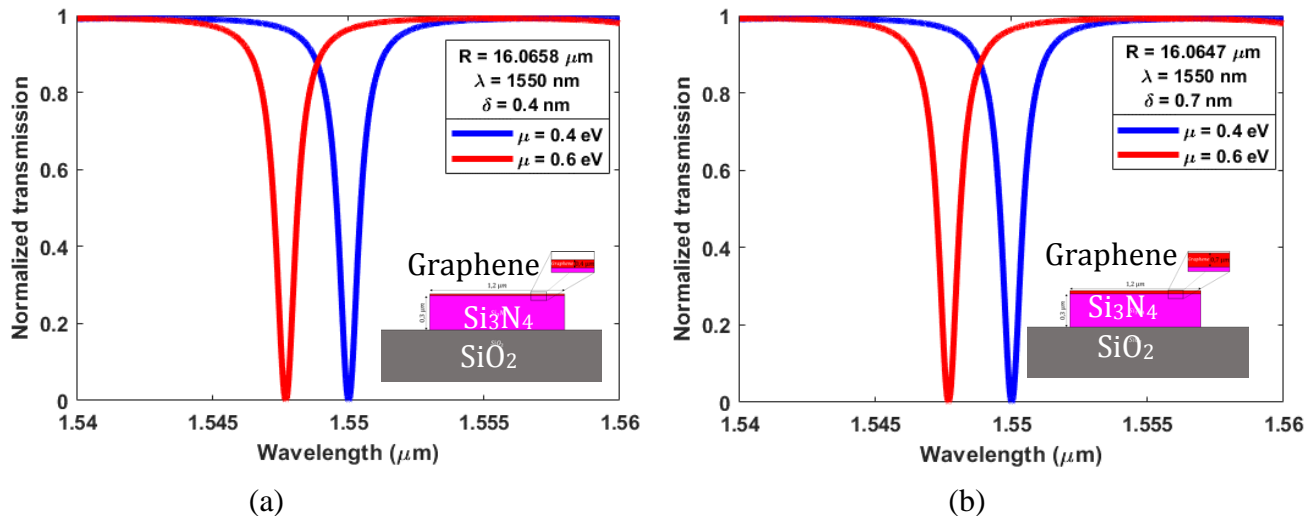

Fig. 8 (a) drop-port transmission spectra of a micro-ring-resonator-based add–drop filter. For a radius R = 16.0658 μm, α = 2 cm−1, and coupling coefficients $\kappa = 0.4$ for $\lambda = 1550\ nm$ and a 0.4 nm thick graphene flake (b) Fig. 11 (a) drop-port transmission spectra of a micro-ring-resonator-based add–drop filter. For a radius R = 16.0658 μm, α = 2 cm−1, and coupling coefficients $\kappa = 0.4$ for $\lambda = 1550\ nm$ and a 0.7 nm thick graphene flake

5   CONCLUSIONS

In this paper, we have demonstrated two different methods for large-scale integration of 2D materials on silicon platform. Accurate areas of deposition have been achieved. A complete theoretical study has been developed to demonstrate how the different 2D material thicknesses can affect the effective refractive index of a TE mode of a 1.2x0.3 μm Si_3N_4 waveguide for the visible range. A finite-difference frequency-domain approach and the Transfer Matrix Method were used in order to mathematically describe different add-drop filters. Modifying the thickness and width of a WS_2 flake, a 0.13% shift in the resonance of the add-drop filter is achieved. An improvement in the resonance shift was observed having changed the material to graphene. Modifying the thickness and width of the graphene flakes deposited on the top of the waveguides up to 8 nm thick and 1.2 μm wide, a 0.23% shift in the resonance of the micro-ring resonator structure is achieved. Approximately, the same shift in resonance is achieved for MoS_2, increasing the thickness of the flake up to approximately half that of the graphene (3.8 nm) and with the same width of 1.2 μm. Finally, active, reconfigurable, graphene-based micro-ring resonators have been studied for optical communications applications in the NIR range, a parametric sweep of the Fermi level has been obtained for different thicknesses of the graphene flakes (0.4 and 0.7nm) and a shift in the resonance of the add-drop filter of 0.148% for a modification in the Fermi level of 0.2 eV was determined, achieving a sensitivity of 1.15% for the device. The difference in the thickness of the graphene should be greater in order to obtain a significant difference in the quality factor and consequently in the sensitivity. Using liquid exfoliated graphene gives us more freedom with the thickness and consequently with the sensitivity of the devices. Nevertheless, using CVD graphene, the difference in the thickness will be negligible for the performance of the proposed devices.

ACKNOWLEDGMENTS

REFERENCES

[1]   Ikeda, K., Saperstein, R. E., Alic, N. and Fainman, Y., "Thermal and Kerr nonlinear properties of plasma-deposited silicon nitride/ silicon dioxide waveguides," Opt. Express **16**(17), 12987 (2008).

[2]   Milgram, J. N., Wojcik, J., Mascher, P. and Knights, a P., "Optically pumped Si nanocrystal emitter integrated with low loss silicon nitride waveguides.," Opt. Express **15**(22), 14679–14688 (2007).

[3]   Gaugiran, S., Gétin, S., Fedeli, J., Colas, G., Fuchs, a, Chatelain, F. and Dérouard, J., "Optical manipulation of microparticles and cells on silicon nitride waveguides.," Opt. Express **13**(18), 6956–6963 (2005).

[4]   Abdollahi Shiramin, L. and Van Thourhout, D., "Graphene Modulators and Switches Integrated on Silicon and Silicon Nitride Waveguide," IEEE J. Sel. Top. Quantum Electron. **23**(1) (2017).

[5]   Han, G. H., Chae, S. J., Kim, E. S., Güneş, F., Lee, I. H., Lee, S. W., Lee, S. Y., Lim, S. C., Jeong, H. K., Jeong, M. S. and Lee, Y. H., "Laser thinning for monolayer graphene formation: Heat sink and interference effect," ACS Nano **5**(1), 263–268 (2011).

[6]   Gutiérrez, H. R., Perea-López, N., Elías, A. L., Berkdemir, A., Wang, B., Lv, R., López-Urías, F., Crespi, V. H., Terrones, H. and Terrones, M., "Extraordinary room-temperature photoluminescence in triangular WS 2 monolayers," Nano Lett. **13**(8), 3447–3454 (2013).

[7]   Reed, G. T., Mashanovich, G., Gardes, F. Y. and Thomson, D. J., "Silicon optical modulators," Nat. Publ. Gr. **4**(8), 518–526 (2010).

[8]   Novoselov, K. S., Geim, A. K., Morozov, S. V, Jiang, D., Zhang, Y., Dubonos, S. V, Grigorieva, I. V and Firsov, A. A., "Electric Field Effect in Atomically Thin Carbon Films," Science (80-.). **306**(5696), 666–669 (2004).

[9]   Li, X., Magnuson, C. W., Venugopal, A., An, J., Suk, J. W., Han, B., Borysiak, M., Cai, W., Velamakanni, A., Zhu, Y., Fu, L., Vogel, E. M., Voelkl, E., Colombo, L. and Ruoff, R. S., "Graphene Films with Large Domain Size by a Two-Step Chemical Vapor Deposition Process," Nano Lett. **10**(11), 4328–4334 (2010).

[10]   Reina, A., Jia, X., Ho, J., Nezich, D., Son, H., Bulovic, V., Dresselhaus, M. S. and Kong, J., "Supporting Information Large Area , Few-Layer Graphene Films on Arbitrary Substrates by Chemical Vapor Deposition," Nano Lett. **9**(1), 1–8 (2009).

[11]   Sun, Z., Yan, Z., Yao, J., Beitler, E., Zhu, Y. and Tour, J. M., "Growth of graphene from solid carbon sources," Nature **468**(7323), 549–552 (2010).

[12]   Wei, D., Liu, Y., Wang, Y., Zhang, H., Huang, L. and Yu, G., "Synthesis of N-Doped Graphene by Chemical Vapor Deposition and Its Electrical Properties," Nano Lett. **9**(5), 1752–1758 (2009).

[13]   Obraztsov, A. N., "Making graphene on a large scale," Nat. Nanotechnol. **4**(April), 212–213 (2009).

[14]   Behabtu, N., Lomeda, J. R., Green, M. J., Higginbotham, A. L., Sinitskii, A., Kosynkin, D. V, Tsentalovich, D., Parra-Vasquez, A. N. G., Schmidt, J., Kesselman, E., Cohen, Y., Talmon, Y., Tour, J. M. and Pasquali, M., "Spontaneous high-concentration dispersions and liquid crystals of graphene.," Nat. Nanotechnol. **5**(6), 406–411 (2010).

[15]   Hernandez, Y., Nicolosi, V., Lotya, M., Blighe, F. M., Sun, Z., De, S., McGovern, I. T., Holland, B., Byrne, M., Gun'Ko, Y. K., Boland, J. J., Niraj, P., Duesberg, G., Krishnamurthy, S., Goodhue, R., Hutchison, J., Scardaci, V., Ferrari, A. C. and Coleman, J. N., "High-yield production of graphene by liquid-phase exfoliation of graphite.," Nat. Nanotechnol. **3**(9), 563–568 (2008).

[16]   Lotya, M., King, P. J., Khan, U., De, S. and Coleman, J. N., "High-concentration, surfactant-stabilized graphene dispersions.," ACS Nano **4**(6), 3155–3162 (2010).

[17]   O'Neill, A., Khan, U., Nirmalraj, P. N., Boland, J. and Coleman, J. N., "Graphene Dispersion and Exfoliation in Low Boiling Point Solvents," J. Phys. Chem. C **115**(13), 5422–5428 (2011).

[18]   Hogan, B. T., Dyakov, S. A., Brennan, L. J., Younesy, S., Perova, T. S., Gun'ko, Y. K., Craciun, M. F. and Baldycheva, A., "Dynamic in-situ sensing of fluid-dispersed 2D materials integrated on microfluidic Si chip," Sci. Rep. **7**, 42120 (2017).

[19]   Ogino, I., Yokoyama, Y., Iwamura, S. and Mukai, S. R., "Exfoliation of Graphite Oxide in Water without Sonication: Bridging Length Scales from Nanosheets to Macroscopic Materials," Chem. Mater. **26**(10), 3334–3339 (2014).

[20]   Paredes, J. I., Villar-Rodil, S., Martínez-Alonso, A. and Tascón, J. M. D., "Graphene Oxide

Dispersions in Organic Solvents," Langmuir **24**(19), 10560–10564 (2008).

[21] Qi, X., Zhou, T., Deng, S., Zong, G., Yao, X. and Fu, Q., "Size-specified graphene oxide sheets: ultrasonication assisted preparation and characterization," J. Mater. Sci. **49**(4), 1785–1793 (2014).

[22] Zhang, L., Liang, J., Huang, Y., Ma, Y., Wang, Y. and Chen, Y., "Size-controlled synthesis of graphene oxide sheets on a large scale using chemical exfoliation," Carbon N. Y. **47**(14), 3365–3368 (2009).

[23] Peng, L., Xu, Z., Liu, Z., Wei, Y., Sun, H., Li, Z., Zhao, X. and Gao, C., "An iron-based green approach to 1-h production of single-layer graphene oxide," Nat. Commun. **6**, 5716 (2015).

[24] Kim, D. W., Kim, D., Min, B. H., Lee, H. and Jung, H.-T., "Sonication-free dispersion of large-area graphene oxide sheets using internal pressure from release of intercalated carbon dioxide," Carbon N. Y. **88**, 126–132 (2015).

[25] Sun, X., Luo, D., Liu, J. and Evans, D. G., "Monodisperse Chemically Modified Graphene Obtained by Density Gradient Ultracentrifugal Rate Separation," ACS Nano **4**(6), 3381–3389 (2010).

[26] Shen, T.-Z., Hong, S.-H. and Song, J.-K., "Effect of centrifugal cleaning on the electro-optic response in the preparation of aqueous graphene-oxide dispersions," Carbon N. Y. **80**, 560–564 (2014).

[27] Zhang, W., Zou, X., Li, H., Hou, J., Zhao, J., Lan, J., Feng, B. and Liu, S., "Size fractionation of graphene oxide sheets by the polar solvent-selective natural deposition method," RSC Adv. **5**(1), 146–152 (2015).

[28] Wang, X., Bai, H. and Shi, G., "Size Fractionation of Graphene Oxide Sheets by pH-Assisted Selective Sedimentation," J. Am. Chem. Soc. **133**(16), 6338–6342 (2011).

[29] Hogan, B. T., Kovalska, E., Craciun, M. F. and Baldycheva, A., "2D material liquid crystals for optoelectronics and photonics," J. Mater. Chem. C **5**(43), 11185–11195 (2017).

[30] Kuzmenko, A. B., Van Heumen, E., Carbone, F. and Van Der Marel, D., "Universal optical conductance of graphite," Phys. Rev. Lett. **100**(11), 2–5 (2008).

[31] Nair, R. R., Blake, P., Grigorenko, A. N., Novoselov, K. S., Booth, T. J., Stauber, T., Peres, N. M. R. and Geim, A. K., "Fine Structure Constant Defines Visual Transparency of Graphene," Science (80-.). **320**(5881), 1308–1308 (2008).

[32] Wang, F., Zhang, Y., Tian, C., Girit, C., Zettl, A., Crommie, M. and Shen, Y. R., "Gate-Variable Optical Transitions in Graphene," Science (80-.). **320**(5873), 206–209 (2008).

[33] Chen, C.-F., Park, C.-H., Boudouris, B. W., Horng, J., Geng, B., Girit, C., Zettl, A., Crommie, M. F., Segalman, R. A., Louie, S. G. and Wang, F., "Controlling inelastic light scattering quantum pathways in graphene," Nature **471**(7340), 617–620 (2011).

[34] Poon, J. K. S., Scheuer, J., Mookherjea, S., Paloczi, G. T., Huang, Y. Y. and Yariv, A., "Matrix analysis of microring coupled-resonator optical waveguides," Opt. Express **12**(1), 90–103 (2004).

[35] Hu, X. and Wang, J., "High Figure of Merit Graphene Modulator Based on Long-Range Hybrid Plasmonic Slot Waveguide," IEEE J. Quantum Electron. **53**(3) (2017).

[36] Chang, Y., Liu, C., Zhong, Z. and Norris, T. B., "Extracting the complex optical conductivity of true two- dimensional layers by ellipsometry," 3–4 (2014).

[37]   Bao, Q. and Loh, K. P., "Graphene photonics, plasmonics, and broadband optoelectronic devices," ACS Nano **6**(5), 3677–3694 (2012).